Hybrid photonic crystal cavity and waveguide for coupling to diamond NV-centers

Paul E. Barclay, Kai-Mei Fu, Charles Santori and Raymond G. Beausoleil

Hewlett-Packard Laboratories, 1501 Page Mill Road, Palo Alto CA 94304

phone: (650) 857-6119, e-mail: paul.barclay@hp.com

Abstract: A design for an ultra-high Q photonic crystal nanocavity engineered to interact with nitrogen-vacancy (NV) centers located near the surface of a single crystal diamond sample is presented. The structure is based upon a nanowire photonic crystal geometry, and consists of a patterned high refractive index thin film, such as gallium phosphide (GaP), supported by a diamond substrate. The nanocavity supports a mode with quality factor $Q > 1.5 \times 10^6$ and mode volume $V < 0.52(\lambda/n_{\mathrm{GaP}})^3$, and promises to allow Purcell enhanced collection of spontaneous emission from an NV located more than 50 nm below the diamond surface. The nanowire photonic crystal waveguide can be used to efficiently couple light into and out of the cavity, or as an efficient broadband collector of NV phonon sideband emission. The proposed structures can be fabricated using existing materials and processing techniques.

References and links

1. A. Gruber, A. Dräbenstedt, C. Tietz, L. Fleury, J. Wratchtrup, and C. v. Borczyskowski, "Scanning confocal optical microscopy and magnetic resonance on single defect centers," Science **276**, 2012–2014 (1997).
2. C. Kurtsiefer, S. Mayer, P. Zarda, and H. Weinfurter, "Stable solid-state source of single photons," Phys. Rev. Lett. **85**, 290 (2000).
3. A. Beveratos, R. Brouri, T. Gacoin, J.-P. Poizat, and P. Grangier, "Nonclassical radiation from diamond nanocrystals," Phys. Rev. A **64**, 061 802 (2001).
4. C. Santori, P. Tamarat, P. Neumann, J. Wrachtrup, D. Fattal, R. G. Beausoleil, J. Rabeau, P. Olivero, A. D. Greentree, S. Prawer, F. Jelezko, and P. Hemmer, "Coherent Population Trapping of Single Spins in Diamond under Optical Excitation," Phys. Rev. Lett. **97**, 247 401 (2006).
5. F. Jelezko, T. Gaebel, I. Popa, A. Gruber, and J. Wrachtrup, "Observation of Coherent Oscillations in a Single Electron Spin," Phys. Rev. Lett. **92**, 076 401 (2004).
6. M. V. Gurudev Dutt, L. Childress, L. Jiang, E. Togan, J. Maze, F. Jelezko, A. S. Zibrov, P. R. Hemmer, and M. D. Lukin, "Quantum Register Based on Individual Electronic and Nuclear Spin Qubits in Diamond," Science **316**, 1312–1316 (2007).
7. L. Childress, M. V. Gurudev Dutt, J. M. Taylor, A. S. Zibrov, F. Jelezko, J. Wrachtrup, P. R. Hemmer, and M. D. Lukin, "Coherent Dynamics of Coupled Electron and Nuclear Spin Qubits in Diamond," Science **314**, 281–285 (2006).
8. L. Childress, J. M. Taylor, A. S. Sørensen, , and M. D. Lukin, "Fault-Tolerant Quantum Communication Based on Solid-State Photon Emitters," Phys. Rev. Lett. **96**, 070 504 (2006).
9. S. C. Benjamin, B. W. Lovett, and J. M. Smith, "Prospects for measurement-based quantum computing with solid state spins," arXiv:0901.3092v2 [quant-ph] (2009).

10. C.-H. Su, A. D. Greentree, and L. C. L. Hollenberg, "Towards a picosecond transform-limited nitrogen-vacancy based single photon source," Opt. Express **16**, 6240–6250 (2008).

11. A. Young, C. Y. Hu, L. Marseglia, J. P. Harrison, J. L. OBrien, and J. G. Rarity, "Cavity enhanced spin measurement of the ground state spin of an NV center in diamond," New J. Phys. **11**, 013 007 (2009).

12. O. Painter, R. K. Lee, A. Yariv, A. Scherer, J. D. O'Brien, P. D. Dapkus, and I. Kim, "Two-Dimensional Photonic Band-Gap Defect Mode Laser," Science **284**, 1819–1824 (1999).

13. Y. Akahane, T. Asano, B.-S. Song, and S. Noda, "High-Q photonic nanocavity in a two-dimensional photonic crystal," Nature **425**, 944–947 (2003).

14. K. Srinivasan, P. E. Barclay, M. Borselli, and O. Painter, "Optical-fiber based measurement of an ultra-small volume high-Q photonic crystal microcavity," Phys. Rev. B **70**, 081 306(R) (2004).

15. B.-S. Song, S. Noda, T. Asano, and Y. Akahane, "Ultra-high-Q photonic double-heterostructure nanocavity," Nature Materials **4**, 207–210 (2005).

16. Y. Takahashi, H. Hagino, Y. Tanaka, B.-S. Song, T. Asanoa, , and S. Noda, "High-Q nanocavity with a 2-ns photon lifetime," Opt. Express **15**, 17 206–17 213 (2007).

17. T. Yoshie, A. Scherer, J. Hendrickson, G. Khitrova, H. Gibbs, G. Rupper, C. Ell, O. Shchekin, and D. Deppe, "Vacuum Rabi splitting with a single quantum dot in a photonic crystal nanocavity," Nature **432**, 200–203 (2004).

18. K. Hennessy, A. Badolato, M. Winger, D. Gerace, M. Atature, S. Gulde, S. Faelt, E. L. Hu, and A. Imamoglu, "Quantum nature of a strongly coupled single quantum dot-cavity system," Nature **455**, 896–899 (2007).

19. D. Englund, A. Faraon, I. Fushman, N. Stoltz, P. Petroff, and J. Vučković, "Controlling cavity reflectivity with a single quantum dot," Nature **450**, 857–861 (2007).

20. Y.-S. Park, A. K. Cook, and H. Wang, "Cavity QED with Diamond Nanocrystals and Silica Microspheres," Nano Lett. **6**, 2075–2079 (2006).

21. P. E. Barclay, O. Painter, C. Santori, K.-M. Fu, and R. Beausoleil, "Coherent interference effects in a nano-assembled optical cavity-QED system," Opt. Express **19**, 8081 (2009).

22. S. Schietinger, T. Schroder, and O. Benson, "One-by-One Coupling of Single Defect Centers in Nanodiamonds to High-Q Modes of an Optical Microresonator," Nano Lett. **8**, 3911–3915 (2008).

23. C. F. Wang, Y.-S. Choi, J. C. Lee, E. L. Hu, J. Yang, and J. E. Butler, "Observation of whispering gallery modes in nanocrystalline diamond microdisks," Appl. Phys. Lett. **90**, 081 110 (2007).

24. C. F. Wang, R. Hanson, D. D. Awschalom, E. L. Hu, T. Feygelson, J. Yang, and J. E. Butler, "Fabrication and characterization of two-dimenstional photonic crystal microcavities in nanocrystalline diamond," Appl. Phys. Lett. **91**, 201 112 (2007).

25. Y. Shen, T. M. Sweeney, and H. Wang, "Zero-phonon linewidth of single nitrogen vacancy centers in diamond nanocrystals," Phys. Rev. B **77**, 033 201 (2008).

26. P. Tamarat, T. Gaebel, J. R. Rabeau, M. Khan, A. D. Greentree, H. Wilson, L. C. L. Hollenberg, S. Prawer, P. Hemmer, F. Jelezko, and J. Wrachtrup, "Stark Shift Control of Single Optical Centers in Diamond," Phys. Rev. Lett. **97**, 083 002 (2006).

27. S. Tomljenovic-Hanic, M. Steel, C. de Sterke, and J. Salzman, "Diamond based photonic crystal microcavities," Opt. Express **14**, 3556–3562 (2006).

28. C. Kreuzer, J. Riedrich-Mller, E. Neu, and C. Becher, "Design of Photonic Crystal Microcavities in Diamond Films," Opt. Express **16**, 1632–1644 (2008).

29. B. A. Fairchild, P. Olivero, S. Rubanov, A. D. Greentree, F. Waldermann, I. W. Robert A. Taylor and, J. M. Smith, S. Huntington, B. C. Gibson, D. N. Jamieson, and S. Prawer, "Fabrication of Ultrathin Single-Crystal Diamond Membranes," Adv. Mater. **20**, 4793–4798 (2008).

30. K.-M. C. Fu, C. Santori, P. E. Barclay, I. Aharonovich, S. Prawer, N. Meyer, A. M. Holm, and R. G. Beausoleil, "Coupling of nitrogen-vacancy centers in diamond to a GaP waveguide," Appl. Phys. Lett. **93**, 234 107 (2008).

31. A. R. M. Zain, N. P. Johnson, M. Sorel, and R. M. D. L. Rue, "Ultra high quality factor one dimensional photonic crystal/photonic wire micro-cavities in silicon-on-insulator (SOI)," Opt. Express **16**, 12 084–12 089 (2008).

32. I. Bayn and J. Salzman, "Ultra high-Q photonic crystal nanocavity design: The effect of a low-ε slab material," Opt. Express **16**, 4972–4980 (2008).

33. K. Rivoire, A. Faraon, and J. Vučković, "Gallium phosphide photonic crystal nanocavities in the visible," Appl. Phys. Lett. **93**, 063 103 (2008).

34. S. G. Johnson, P. R. Villeneuve, S. Fan, and J. D. Joannopoulos, "Linear waveguides in photonic-crystal slabs," Phys. Rev. B **62**, 8212–8222 (2000).

35. P. Lalanne, "Electromagnetic Analysis of Photonic Crystal Waveguides Operating Above the Light Cone," IEEE J. Quantum Electron. **38**, 800–804 (2002).

36. K. Srinivasan and O. Painter, "Momentum Space Design of High-Q Photonic Crystal Nanocavities in Two-Dimensional Slab Waveguides," Opt. Express **10**, 670–684 (2002). http://www.opticsexpress.org/abstract.cfm?URI=OPEX-10-15-670

37. O. Painter and K. Srinivasan, "Localized defect states in two-dimensional photonic crystal slab waveguides: A simple model based upon symmetry analysis," Phys. Rev. B **68**, 035 110 (2003).

38. All FDTD simulations used the MEEP software package. http://ab-initio.mit.edu/wiki/index.php/Meep

39. P. Velha, J. C. Rodier, P. Lalanne, J. P. Hugonin, D. Peyrade, E. Picard, T. Charvolin, and E. Hadji, "Ultra-high-reflectivity photonic-bandgap mirrors in a ridge SOI waveguide," New J. Phys. **8**, 204 (2006).
40. A. W. Snyder and J. D. Love, *Optical Waveguide Theory* (Chapman and Hall, New York, NY, 1983).
41. E. Istrate and E. H. Sargent, "Photonic crystal heterostructures and interfaces," Rev. Mod. Phys. **78**, 455 (2006).
42. M. Notomi, E. Kuramochi, and H. Taniyama, "Ultrahigh-Q Nanocavity with 1D Photonic Gap," Opt. Express **16**, 11 095 (2008).
43. J. S. Foresi, P. R. Villeneuve, J. Ferrera, E. R. Thoen, G. Steinmeyer, S. Fan, J. D. Joannopoulos, L. C. Kimerling, H. I. Smith, and E. P. Ippen, "Photonic-Bandgap microcavities in optical waveguides," Nature **390**, 143–145 (1997).
44. A. Jugessur, P. Pottier, and R. De La Rue, "One-dimensional periodic photonic crystal microcavity filters with transition mode-matching features, embedded in ridge waveguides," Electron. Lett. **39**, 367 – 369 (2003).
45. M. W. McCutcheon and M. Lončar, "Design of an ultrahigh Quality factor silicon nitride photonic crystal nanocavity for coupling to diamond nanocrystals," Opt. Express **16**, 19 136 (2008).
46. J. Chan, M. Eichenfield, R. Camacho, and O. Painter, "Optical and mechanical design of a zipper photonic crystal optomechanical cavity," Opt. Express **17**, 3802–3817 (2009).
47. O. Painter, K. Srinivasan, and P. E. Barclay, "Wannier-like equation for the resonant cavity modes of locally perturbed photonic crystals," Phys. Rev. B **68**, 035 214 (2003).
48. P. E. Barclay, K. Srinivasan, and O. Painter, "Design of photonic crystal waveguides for evanescent coupling to optical fiber tapers and integration with high-Q cavities," J. Opt. Soc. Amer. B **20**, 2274–2284 (2003).
49. D. Morie and T. Baba, "Dispersion-controlled optical group delay device by chirped photonic crystal waveguides," Appl. Phys. Lett. **85**, 1101–1103 (2004).
50. P. Lalanne, S. Mias, and J. P. Hugonin, "Two physical mechanisms for boosting the quality factor to cavity volume ratio of photonic crystal microcavities," Opt. Express **12**, 458–467 (2004).
51. C. Sauvan, G. Lecamp, P. Lalanne, and J. Hugonin, "Modal-reflectivity enhancement by geometry tuning in Photonic Crystal microcavities," Opt. Express **13**, 245–255 (2005).
52. N. B. Manson, J. P. Harrison, and M. J. Sellars, "Nitrogen-vacancy center in diamond: Model of the electronic structure and associated dynamics," Phys. Rev. B **74**, 104 303 (2006).
53. H. J. Kimble, "Strong Interactions of Single Atoms and Photons in Cavity QED," Phys. Scr. **T76**, 127–137 (1998).
54. C. Santori, P. E. Barclay, K.-M. C. Fu, and R. G. Beausoleil, "Vertical distribution of nitrogen-vacancy centers in diamond formed by ion implantation and annealing," Phys. Rev. B **79**, 125 313 (2009).
55. V. S. C. Manga Rao and S. Hughes, "Single Quantum Dot Spontaneous Emission in a Finite-Size Photonic Crystal Waveguide: Proposal for an Efficient "On Chip" Single Photon Gun," Phys. Rev. Lett. **99**, 193 901 (2007).
56. E. Yablonovitch, D. Hwang, T. J. Gmitter, L. T. Florez, and J. P. Harbison, "Van der Waals bonding of GaAs epitaxial liftoff films onto arbitrary substrates," Appl. Phys. Lett. **56**, 2419–2421 (1990).
57. P. E. Barclay, C. Santori, K.-M. Fu, and R. G. Beausoleil, "Microcavities for cavity-QED in single crystal diamond," in *Conference on Lasers and Electro-Optics/International Quantum Electronics Conference Proceedings* p. IMF3 (2009).
58. G. Davies, S. C. Lawson, A. T. Collins, A. Mainwood, and S. J. Sharp, "Vacancy-related centers in diamond," Phys. Rev. B **46**, 13 157–13 170 (1992).
59. J. Meijer, B. Burchard, M. Domhan, C. Wittmann, T. Gaebel, I. Popa, F. Jelezko, and J. Wrachtrup, "Generation of single color centers by focused nitrogen implantation," Applied Physics Letters **87**, 261 909 (2005).
60. F. Waldermann, P. Olivero, J. Nunn, K. Surmacz, Z. Wang, D. Jaksch, R. Taylor, I. Walmsley, M. Draganski, P. Reichart, A. Greentree, D. Jamieson, and S. Prawer, "Creating diamond color centers for quantum optical applications," Diamond and Related Materials **16**, 1887 – 1895 (2007).

1. Introduction

Nitrogen-vacancy (NV) centers found in diamond are a promising system for realizing optically addressable solid-state spin qubits. In single-crystal diamond, negatively charged NV^- centers have been used in a number of experimental demonstrations relevant to quantum information processing, including single photon generation [1, 2, 3], coherent population trapping [4], and optical readout and manipulation of single nuclear spins [5, 6, 7]. In order to utilize these properties in quantum information processing applications [8, 9], efficient and scalable optical coupling between NVs and photonic devices such as waveguides and microcavities [10, 11] is necessary. Photonic crystal nanocavities [12, 13, 14, 15, 16] confine photons to sub-wavelength mode volumes, V, enabling Purcell enhanced coupling between an optical dipole, such as an NV-center or quantum dot, and the cavity mode [17, 18, 19]. The coherent dipole cavity coupling rate scales as $1/\sqrt{V}$, and small V is particularly beneficial in cavity-QED (Quantum

Electrodynamic) systems where intrinsic optical loss or dipole dephasing rates are large.

Recently, optical coupling between high-Q microcavities and NVs hosted in diamond nanocrystals has been reported [20, 21, 22], and devices for studying NVs hosted in nanocrystalline diamond films have been fabricated [23, 24]. However, to-date many desirable properties of NVs in single-crystal diamond have not yet been observed in nanocrystalline diamond. Although spontaneous lifetime-limited optical transition linewidths have been measured in single NVs hosted in diamond nanocrystals, they exhibit ~ 10 THz inhomogeneous broadening and have not been measured in high yield from an ensemble of candidate nanocrystals [25]. In bulk single crystal diamond, NV$^-$ optical transitions with lifetime limited linewidths [26], inhomogeneous broadening of less than 10 GHz, and time-averaged spectral diffusion below 100 MHz [4] have been observed. Because of the superior properties of NVs in bulk single crystal diamond, some cavity geometries using only single-crystal diamond and air have been proposed [27, 28]. However, there are difficulties in fabricating photonic devices from single-crystal diamond, since vertical optical confinement within the diamond requires either a three dimensional etching process, or a method for fabricating thin single-crystal diamond films [29].

An alternative to fabricating devices directly from single-crystal diamond is to integrate a patterned high-index optical waveguiding layer on top of a diamond substrate, from which photons can couple evanescently to NVs close to the diamond surface. Recently, a hybrid GaP-diamond material system, consisting of an optically thin GaP film attached to a diamond substrate, was used to demonstrate optical coupling between NVs close to the diamond surface and ridge waveguides patterned in the GaP film [30]. Owing to the enhanced local density of states in the near field of the GaP waveguide modes, relatively efficient evanescent coupling between NVs and the GaP waveguide can be achieved. In order to efficiently couple to individual NVs, three dimensional confinement provided by an optical cavity is necessary. Here we present designs for a GaP-diamond photonic crystal nanowire waveguide and nanocavity which can be fabricated using available materials and processing techniques. Using numerical simulations, we study the sensitivity of the optical properties of these devices on structural parameters. We also simulate the coupling of spontaneous emission from a broadband source, such as phonon sideband emission from an NV-center, into the proposed waveguide design, and show that efficient broadband collection of NV emission is possible with these structures.

2. Hybrid GaP-Diamond photonic crystal nanocavity

Photonic crystal nanocavities, formed by introducing localized perturbations to planar periodic structures, can support ultra-high Q/V resonances. Ultra-high Q/V devices have been demonstrated at near-IR wavelengths in free standing membranes such as Si with $Q > 2.5 \times 10^6$ [16]. In Si films supported by low-index SiO$_2$ substrates (SOI), devices with $Q > 1.5 \times 10^5$ have been realized [31]. Although simulations of photonic crystal cavities fabricated from diamond membranes ($n_{\text{Dia}} \sim 2.4$) predict radiation loss limited resonances with $Q > 10^6$ [27, 28, 32], material loss has limited $Q < 600$ [24] in nanocavities fabricated from nanocrystalline membranes. Photonic crystal nanocavities fabricated from single crystal diamond membranes [29] have not yet been demonstrated.

Here we study photonic crystal cavities formed in a thin waveguiding layer supported by a diamond substrate hosting high quality NVs near the diamond surface, as indicated in Fig. 1. In choosing a film from which to form the waveguide layer, we are limited to materials which are transparent at the NV$^-$ zero phonon transition wavelength, $\lambda_{\text{NV}^-} = 637$nm, and whose refractive index exceeds n_{Dia}. Epitaxially grown GaP films have a nominally high refractive index ($n_{\text{GaP}} \sim 3.3 > n_{\text{Dia}}$) and low optical absorption at λ_{NV^-}. Photonic crystal cavities formed in GaP membranes have recently been demonstrated with $Q \sim 1700$ [33], and in Ref. [30], optical loss of ~ 72 dB/cm was measured in a GaP waveguide supported by a single crystal diamond
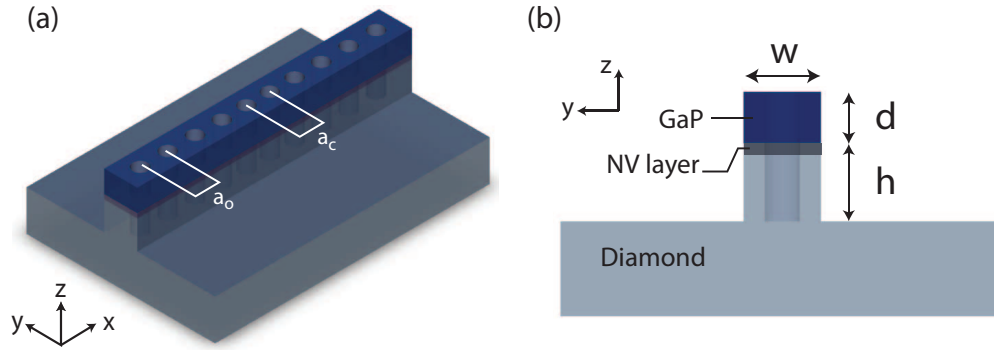
Fig. 1. Schematic of the GaP-on-diamond photonic crystal cavity design. (a) Isometric view, (b) end view. For the optimized structure studied in this paper, $[w, d, h] = [192, 128, 640]$ nm, $[a_o, a_c] = [160, 141]$ nm (tapered over 6 periods), and the hole radius $r = 43$ nm.

substrate. The waveguide loss measurements presented in Ref. [30] indicate that devices with absorption and surface scattering limited $Q > 2 \times 10^4$ can be realized in this system. With improved processing to reduce scattering loss, it is expected that material loss limited Q exceeding this value should be possible.

Realizing a high-Q photonic crystal nanocavity in this GaP-diamond system is complicated by the diamond substrate's moderately high refractive index ($n_{\mathrm{Dia}} \sim 2.4$). Compared to photonic crystal membrane or SOI devices, a diamond substrate expands the light cone into which photons can radiate out of the nanocavity. In addition, the broken vertical mirror symmetry from the diamond substrate precludes the existence of a bound mode in the GaP waveguide layer for arbitrarily low frequencies. As discussed below, the underlying GaP-diamond nanowire waveguide structure from which the nanocavity studied here is realized does not support a non-radiating mode in the wavelength range of interest. This is a result of the subwavelength dimensions of the waveguide cross-section, which provides strong modal confinement at the expense of reducing the effective index of the waveguide modes below n_{Dia}. However, by extending the waveguide sidewalls into the diamond substrate, radiation into the diamond substrate can be made arbitrarily small. As we will show below, for a realistic diamond sidewall height, the proposed structure supports waveguide modes whose radiation loss is smaller than the expected intrinsic material or scattering loss, and forms a low-loss structure for realizing a high-Q nanocavity.

2.1. GaP-diamond photonic crystal nanowire waveguide

The underlying structure of the photonic crystal nanocavity illustrated in Fig. 1 consists of a GaP photonic crystal nanowire waveguide whose sidewalls have been extended into a diamond substrate. This waveguide supports Bloch modes which form the basis for localized resonances formed when the periodic symmetry of the waveguide is broken. In general, the Bloch modes are either leaky or guided, depending on their frequency, ω, and wavenumber, k, relative to the air and diamond lightlines [34, 35]. Waveguide modes with an effective index smaller than that of diamond, $n_{\mathrm{eff}} = k/\omega(k) < n_{\mathrm{Dia}}$ (setting $c = 1$), will leak into the diamond substrate. High-Q cavity resonances are realized by engineering a perturbation which couples guided or low-loss Bloch modes [36, 37]. Using 3-dimensional finite difference time domain (FDTD) simulations [38] to study the photonic crystal waveguide loss, we can predict an upper limit on the Q of a nanocavity formed from this structure.

Figure 2(a) shows the first Brillouin zone of the band-structure for the lowest frequency
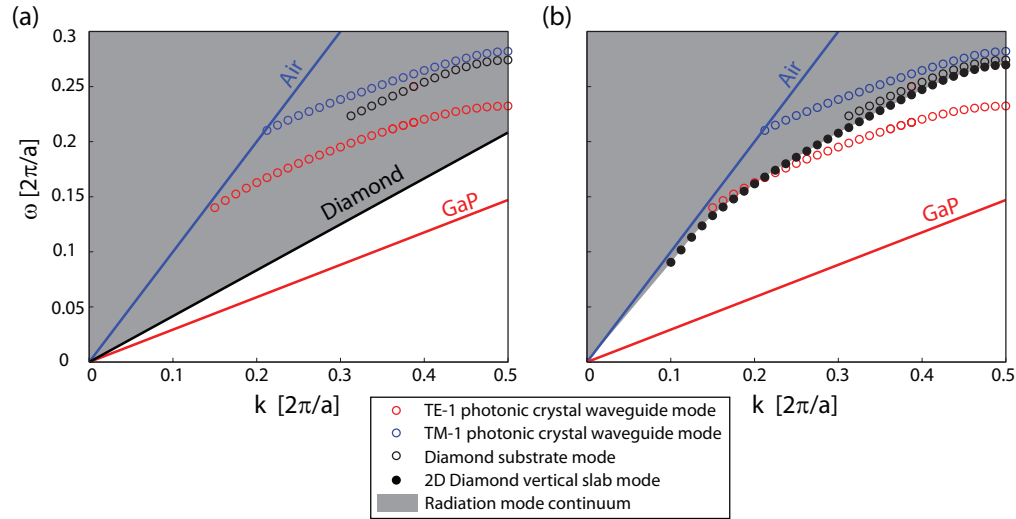
Fig. 2. GaP-diamond photonic crystal waveguide band structure, and GaP, diamond substrate, and air lightlines. Shaded regions indicate the presence of a continuum of lossy radiating modes. In both (a) and (b) the photonic crystal waveguide modes (red and blue points) were calculated for a structure with $h = 640$ nm. The diamond lightline in (a) is that of a bulk diamond substrate. The filled black points in (b) are the lowest frequency E_y polarized modes of an infinitely tall diamond slab of width w patterned with air holes along the vertical axis whose spacing and radius are equal to that of the GaP waveguiding layer.

GaP-diamond photonic crystal nanowire waveguide modes. Also shown are the air, diamond, and GaP lightlines. The calculation used waveguide cross-section dimension $[w, d] = [192, 128]$ nm, hole spacing $a = 160$ nm, and hole radius $r = 43$ nm. The hole spacing was chosen to approximately position the lowest energy waveguide mode band edge in the wavelength range of interest. The waveguide cross-section was not systematically optimized, and when normalized by the hole spacing a, is similar to that used in previous nanowire based cavity designs [31, 39]. r/a was chosen based upon initial simulations of the Q of the nanocavity design studied below in Sec. 2.2, and is also similar to values used in other work. A mesh with resolution $a/20$, perfectly matched layer (PML) boundary conditions in the $\hat{y}$ and $\hat{z}$ directions (320 nm PML layer thickness), and Bloch boundary conditions in the $\hat{x}$ direction were used in these simulations. For clarity, only modes with even parity in the $\hat{y}$ direction are calculated. Odd modes lie higher in frequency, and as will become clear below, we are primarily interested in the lowest frequency waveguide mode. Note that parity in the $\hat{z}$ dimension is not conserved for these GaP-diamond structures, since they are not vertically symmetric. Both the lowest frequency TE-like (dominantly E_y polarized) and TM-like (dominantly H_y polarized) modes are shown in Fig. 2. We label these modes TE-1 and TM-1, respectively. Also evident in Fig. 2(b) is a mode (black open points) whose dispersion lies between the TE-1 and TM-1 bands. This mode corresponds to a leaky mode whose field is predominantly confined within the diamond substrate. Leaky modes with waveguide quality factor, $Q_{wg} < 100$ are not shown. Q_{wg} is related to the waveguide loss per unit length, α, by $\alpha = \omega/Q v_g$, where $v_g = \partial\omega/\partial k$ is the group velocity of the waveguide mode.

From Fig. 2(a), it is immediately clear that for the specified waveguide dimensions, no waveguide modes lie below the diamond lightline. In particular, at the band edge ($k = k_X = \pi/a$) the effective index of the lowest frequency waveguide mode is smaller than n_{Dia}; this mode is
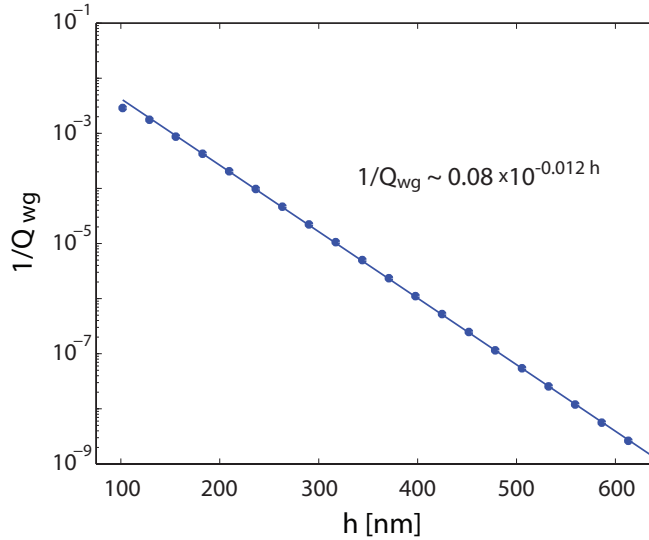
Fig. 3. Dependence of the photon loss rate ($\sim \omega/Q_{\mathrm{wg}}$) of the TE-1 photonic crystal waveguide mode on etch depth, for $k = \pi/a_c$, and hole spacing $a = a_c = 141$ nm).

expected to leak into the diamond substrate. This leakage could be reduced by increasing the GaP waveguide dimensions (w, d), increasing the effective index of the mode at the expense of decreasing the peak single photon field strength, and decreasing the frequency and momentum mismatch between the TE-1 and higher order waveguide modes. Alternatively, we can extend the GaP sidewalls (including the holes) by depth h into the diamond substrate. In the limit that $h \gg \lambda/n_{\mathrm{Dia}}$, the bulk diamond lightline is no longer relevant in determining whether a GaP-diamond waveguide mode is bound or leaky. Instead, the relevant substrate is the approximately two dimensional vertical diamond photonic crystal slab underneath the GaP photonic crystal waveguide. The band-structure of the lowest frequency E_y polarized mode supported by this vertical slab is shown in Fig. 2(b). Above this band exists a continuum of radiating slab modes with non-zero vertical momentum; this band forms a renormalized "structured lightline". At $k = k_X$, the TE-1 mode lies below this structured lightline, indicating that this mode is not leaky in the $h \gg \lambda/n_{\mathrm{Dia}}$ limit. The existence of this mode below the structured lightline is not sensitive to the choice of w, since decreasing w decreases the effective index of both the TE-1 mode and the lowest energy radiating slab mode. Decreasing d decreases the TE-1 effective index in a manner typical of slab and ridge waveguides [40], and can push the TE-1 mode above the structured lightline at a given frequency.

In Fig. 3 the waveguide loss per optical cycle, $1/Q_{\mathrm{wg}}$, of the TE-1 mode is shown as a function of the etch depth h, at $k = k_X$, for $a = a_c = 141$ nm, where a_c is the "cavity" hole spacing of the nanocavity design presented in the following section and indicated in Fig. 1. This was calculated using FDTD simulations, by monitoring the power radiated into the absorbing $\hat{y}$ and $\hat{z}$ boundaries of a waveguide Bloch unit cell. We expect Q_{wg} at $k = k_X$ to place an upper limit on the Q of a cavity mode formed predominantly from the TE-1 mode [37]. Figure 3 indicates that for $h < 100$ nm, the TE-1 waveguide mode is very leaky with $Q_{\mathrm{wg}} < 500$, but that for increased etch depth $h = 600$ nm, the loss can be reduced and $Q_{\mathrm{wg}} > 10^9$. For $h > 100$ nm, Q_{wg} increases exponentially with h.
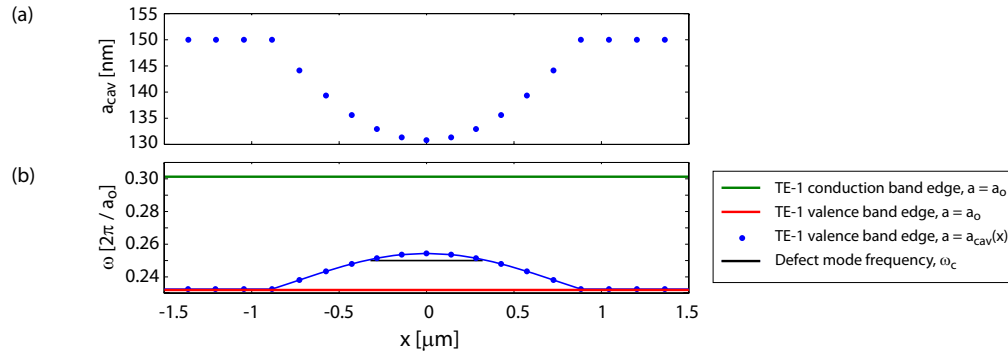
Fig. 4. (a) Lattice constant a_{cav} as a function of position in the cavity. Each point, x_i, on the graph corresponds to a position midway between the center of two holes spaced by $a_{cav}(x_i)$. (b) Frequency of the photonic crystal waveguide TE-1 valence band edge, $\omega_X^{TE\text{-}1} = \omega^{TE\text{-}1}(k_X = \pi/a)$, for a set by the cavity's varying "local" hole spacing, $a_{cav}(x_i)$, shown in (a).

2.2. Nanocavity design

The nanocavity studied here is formed in the photonic crystal nanowire waveguide described in Sec. 2.1 by locally perturbing the hole spacing, a_{cav}, as indicated in Figs. 4(a) and 5(a), forming a heterostructure [41] cavity [15, 42]. The hole spacing is varied slowly over 6 periods from $a_c = 141$ nm in the center of the cavity, to a constant "bulk" value of $a_o = 160$ nm. The cavity is symmetric about the x and y axes. For simplicity, the hole radius remains constant. This type of photonic crystal nanowire waveguide cavity [43, 44] supports localized cavity modes with simulated radiation loss limited $Q > 10^7$ when applied to structures with air undercladding (waveguide-substrate index contrast $\Delta n = n_{SiN} - n_{air} \sim 2.0 - 1.0$) [45, 46]. In SOI material systems ($\Delta n = n_{Si} - n_{SiO_2} \sim 3.48 - 1.44$), nanowire based cavities with $Q > 4 \times 10^5$ have been theoretically studied [39]. Ultrahigh Q/V nanocavities formed in photonic crystal nanowire waveguides on a high-index substrate such as diamond have not been previously investigated.

Adjusting the local hole spacing within the photonic crystal waveguide shifts the frequency range of the photonic crystal waveguide stop-band. In a quasi-1D picture, the photonic crystal waveguide forms an "optical potential" [47] whose band edge is locally modulated by the variation in the hole spacing or hole size [48, 49, 46]. In the cavity design considered here, the local reduction in hole spacing shifts the valence and conduction band edges up in frequency so that the cavity supports an "acceptor" defect mode [34] formed by superpositions of the valence band states of the unperturbed photonic crystal nanowire waveguide [37].

Following an analysis similar to that in Ref. [46], the photonic crystal cavity optical potential is illustrated by Fig. 4(b), which shows the frequency $\omega_X^{TE\text{-}1}$ of the TE-1 valence band edge as a function of the "local" hole spacing, a_{cav}, at positions x_i midway between two holes in the cavity. The band edge frequency $\omega_X^{TE\text{-}1}$ was calculated at each x_i by using FDTD simulations to determine the band structure of the nanowire photonic crystal waveguide in Sec. 2.1, with the hole spacing set to $a_{cav}(x_i)$. Also shown are the frequencies of the TE-1 valence and conduction band edges in the "bulk" waveguide region, where $a = a_o$, and of a high-Q localized cavity mode discussed in detail below. Note that these photonic crystal nanowire cavities have also been analyzed in the context of the unperturbed photonic crystal waveguide sections forming mirrors for photons trapped in the central cavity region [50, 51, 39, 45].

FDTD simulations of this structure predict that it supports a mode at a resonance wavelength
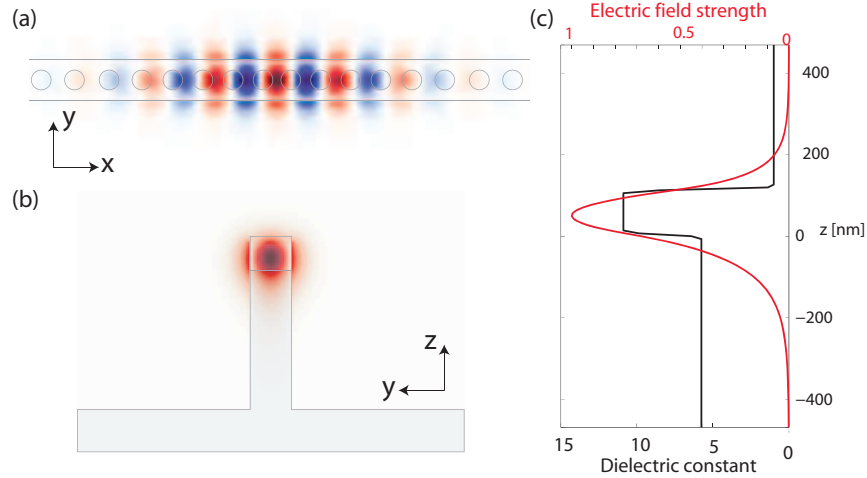
Fig. 5. Dominant electric field component (E_y) of the high-Q nanocavity mode. (a) Top view: $x-y$ plane bisects the GaP waveguiding layer. (b) End view: $y-z$ plane through the center of the cavity. (c) Vertical profile of the field and dielectric constant.

ω_c close to the NV$^-$ zero phonon line at 637nm ($\omega_c = 0.249 \times 2\pi/a_o$), with $Q = 1.5 \times 10^6$ and mode volume $V = 0.52 \left(\lambda/n_{GaP}\right)^3$, where V is defined by the peak electric field energy density: $V = \int n^2|E|^2 d\mathbf{r} / \left(n^2|E|^2\right)_{max}$. The maximum field amplitude inside the diamond is $E_s = 0.72E_o$, where E_o is the field maximum at the location of maximum energy density. E_o is located inside the high index GaP layer for the device and mode studied here. The field maximum decays to $0.10E_o$ at a depth $z = 155$ nm below the diamond surface. Simulations indicate that similar designs with the number of grading periods reduced to 4 support more tightly confined modes ($V \sim 0.3 \left(\lambda/n_{GaP}\right)^3$) with a maximum $Q \sim 6 \times 10^4$. The mesh used in these simulations had uniform resolution $a_o/20$, and extended $N = 8$ periods (a_o) in $\pm\hat{x}$ beyond the end of the graded region, $5a_o$ in $\pm\hat{z}$ above and below the diamond surface, and $3a_o$ along the $\pm\hat{y}$ directions. A PML layer thickness of $4a_o$ was used in the highest-Q simulations. After exciting the structure with a narrow band source, the steady state ratio of stored and radiated power was used to calculate the modal Q. The radiated power along each axis was monitored using reference frames positioned $a_o/2$ away from each PML boundary. Mirror symmetry was enforced about the $\hat{x}$ (odd parity) and $\hat{y}$ (even parity) axes. Higher resolution ($a_o/25$) simulations of the $h = 640$ nm structures were also conducted, and it was verified that the structure supports a mode with $Q > 1.5 \times 10^6$.

The role of the diamond substrate in limiting Q is illustrated by simulating its dependence on the depth of the etched diamond ridge. Figure 6(a) shows Q as a function of h, and indicates the relative contributions to Q due to radiation into the bottom diamond substrate (Q_{bot}), top air cladding (Q_{top}), end of the cavity (Q_{end}) and side of the cavity (Q_{side}). The total cavity Q is given by $Q^{-1} = Q_{top}^{-1} + Q_{bot}^{-1} + Q_{end}^{-1} + Q_{side}^{-1}$. When h is reduced to 160 nm, increased radiation loss into the substrate degrades $Q < 500$. For $h > 640$ nm, radiation loss through the end of the cavity into the photonic crystal waveguide begins to play a non-negligible role in limiting Q.

Figure 6(b) shows the dependence of Q on the number N of waveguide periods between the cavity grading edge and the PML absorbing layer used in the simulation. For $N > 8$, Q_{end} is approximately constant, indicating that it is limited by coupling between the cavity mode and either photonic crystal waveguide modes which do not exhibit a bandgap at ω_c (e.g., the
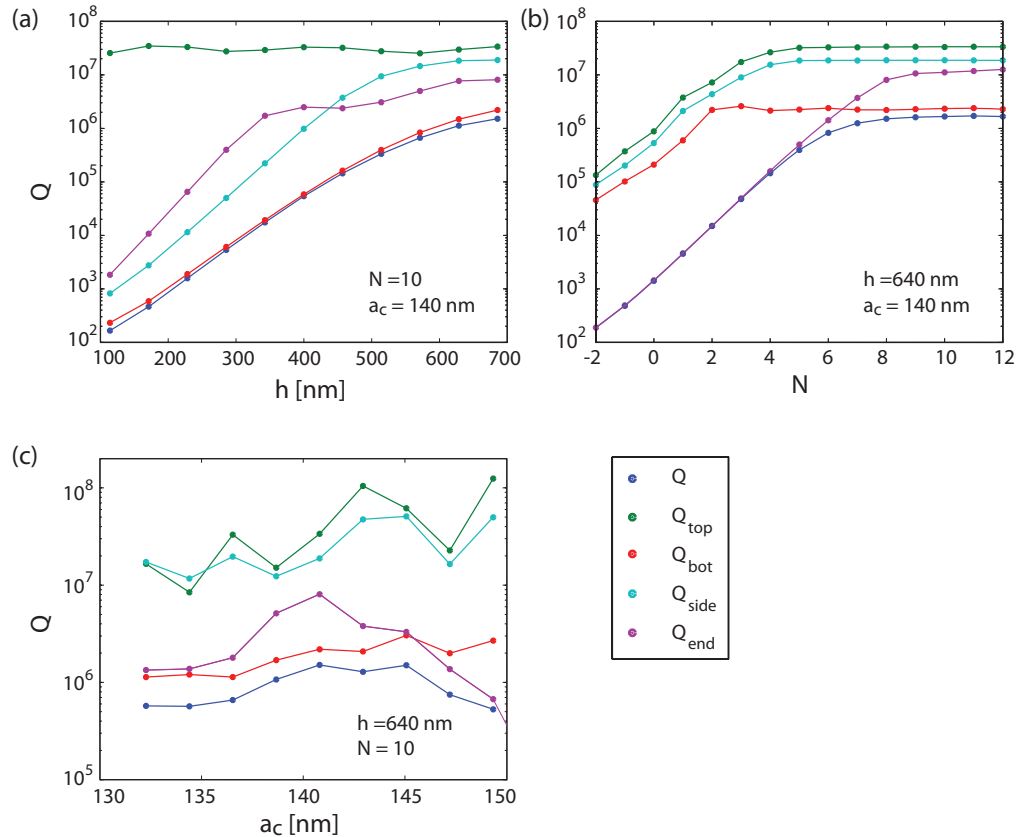
Fig. 6. Dependence of nanocavity mode Q on geometric parameters. The total Q (blue points) and the contribution to Q from radiation into specific directions (other colored points) are given. Dependence of Q on (a) etch depth h, (b) number of "mirror" periods N in the $\hat{x}$ direction between the edge of the graded cavity region and the PML absorbing simulation boundary, (c) cavity minimum (center) hole spacing a_c. For $N < 0$ in (b), the PML boundary of the simulation domain overlaps $|N|$ periods of the graded cavity region.

TM-1 mode) or radiation modes [50, 51]. For $N < 5$, the cavity loss is dominated by "mirror" leakage. In a practical device, N represents the number of "mirror" periods between the edge of the cavity grading and an integrated waveguide, and would be set to a value that ensures that radiation loss from of the cavity is predominantly into the waveguide.

The sensitivity of Q to the central cavity hole spacing, a_c, is shown in Fig. 6(c). When a_c is varied between $132 - 150$ nm, Q remains $> 5 \times 10^5$. In these simulations, the bulk hole spacing is maintained fixed at $a_o = 160$ nm, and the grading of a_c remains parabolic. Q and Q_{end} are maximized when $a_c = 141$ nm, while Q_{bot} trends upward as $a_c \rightarrow a_o$. In this limit, the depth of the parabolic cavity defect becomes increasingly small, minimizing coupling to lossy waveguide modes close to the diamond lightline. As a result, Q_{bot} increases. Q_{end} is maximized when a sufficiently small a_c is chosen to position ω_c well within the TE-1 bandgap, as illustrated in Fig. 4(b). However, pushing ω_c too far above the TE-1 valence band edge can result in efficient phase matched coupling between the cavity mode and the lossy TM-1 valence band edge modes (see Fig. 2), reducing Q_{end}. These competing dependencies determine the

optimum a_c. Note that V varies between $0.42 - 0.70$ $(\lambda/n_{\text{GaP}})^3$ over the simulated range of a_c.

2.3. Nanocavity cavity-QED parameters for coupling to NV$^-$ centers

From the FDTD calculations of V and Q presented above, we can predict the coherent coupling rate, g, for a single NV$^-$ center located near the cavity and coupled to a single photon stored in the nanocavity mode. For experiments in cavity QED we must be careful to distinguish between zero-phonon optical transitions (these become spectrally narrow at low temperature) and phonon-assisted transitions. The total spontaneous emission rate of an NV$^-$ center is measured to be $\gamma_{\text{tot}} = 2\pi \times 13$ MHz; however the rate into the ZPL alone, γ_{ZPL}, is only 3% of γ_{tot} [52]. The coherent coupling rate between a single photon and the NV$^-$ ZPL is given by

$$g_{\text{NV}}/2\pi = \frac{1}{8\pi^2}\sqrt{\frac{3\omega\gamma_{\text{ZPL}}}{\overline{V}}\frac{n_{\text{GaP}}}{n_{\text{Dia}}}}\left|\frac{E(\mathbf{r}_{\text{NV}})}{E_o}\right| \tag{1}$$

where $\overline{V} = V/(\lambda/n_{\text{GaP}})^3$, $|E(\mathbf{r}_{\text{NV}})|$ is the magnitude of the electric field at the NV location, and E_o is the field strength at the electric field energy density maximum, which is located within the GaP for the device studied here. This expression assumes that the spatial orientation of the NV transition dipole moment and electric field polarization are parallel, which is possible for one of four allowed NV orientations in $\langle 111 \rangle$ diamond. For the cavity mode volume given in Sec. 2.2, Eq. (1) gives $g_s/2\pi = 2.25$ GHz for an NV optimally located at the diamond surface.

Assuming that the cavity Q is limited by radiation loss as calculated in Sec. 2.2, we see that $[g_s, \kappa, \gamma_{\text{tot}}]/2\pi = [2.25, 0.16, 0.013]$ GHz, where $\kappa = \omega/2Q$, indicating that it is possible to reach the strong coupling regime [53] using this nanocavity design. Also of interest is the Purcell enhanced spontaneous emission rate of the NV$^-$ ZPL into the cavity mode. Assuming the cavity and NV$^-$ ZPL are aligned spectrally, the Purcell enhancement factor to the ZPL spontaneous emission rate is given by,

$$F = \frac{3}{4\pi^2}\frac{Q}{\overline{V}}\frac{n_{\text{GaP}}}{n_{\text{Dia}}}\left|\frac{E(\mathbf{r}_{\text{NV}})}{E_o}\right|^2\frac{\gamma_{\text{ZPL}}}{\gamma_{\text{tot}}} = \frac{2g_{\text{NV}}^2}{\kappa\gamma_{\text{tot}}}. \tag{2}$$

For an NV optimally positioned at the diamond surface, Eq. (2) gives $F_s = 4.9 \times 10^3$.

In a realistic experiment, it may not be possible to couple to NVs with desirable optical and spin coherence properties arbitrarily close to the diamond surface [54]. In addition, material loss and fabrication imperfections will likely limit the nanocavity Q below the highest values presented in Sec. 2.2. If we assume that the NV is optimally positioned 50 nm below the diamond surface, and that the cavity Q is limited to 2×10^4 (e.g., due to material absorption and surface scattering [30]), we find $F > 16$, indicating that $\sim 94\%$ of the *total* NV$^-$ spontaneous emission will radiate into the nanocavity mode. The 6% of uncoupled NV emission will radiate into phonon sidebands not resonant with the cavity mode.

2.4. Waveguide collection of NV phonon sideband emission

In addition to forming the basic structure for the the nanocavity presented in Sec. 2.2, the waveguide studied in Sec. 2.1 can function as an efficient broadband collector of radiation from NV phonon sidebands. Measurements of broadband phonon-sideband emission are used in experiments to gather information regarding the relative populations of the NV spin triplet ground states [4], as well as the nuclear spin state of neighboring impurities [5, 6, 7]. From coupled-mode theory [40], the normalized power spectral density, $|s(\omega)|^2$, coupled into a waveguide mode from a NV dipole located at position $\mathbf{r}_{\text{NV}}$ in the photonic crystal waveguide near field is approximately given by

$$|s(\omega)|^2 = \frac{3}{8\pi}\left|\frac{E(\mathbf{r}_{\text{NV}})}{E_o}\right|^2\frac{(\lambda/n_{\text{GaP}})^2}{A}\frac{n_g(\omega)}{n_{\text{Dia}}}, \tag{3}$$
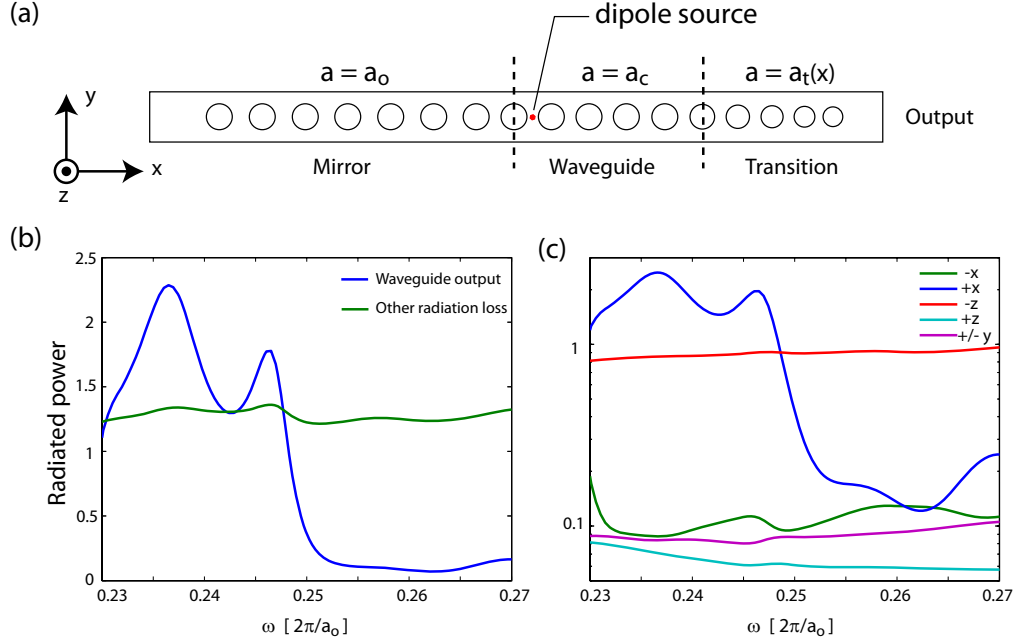
(a)

(b)   (c)

Fig. 7. (a) Geometry of the simulated dipole and the asymmetric photonic crystal waveguide hole pattern. Left of the dipole, the hole spacing is set to a value (a_o) larger than the hole spacing (a_c) to the right of the dipole. For frequencies close to the valence band edge $\omega_X^{\text{TE-1}}$ of the right waveguide region, there are no propagating waveguide modes to the left of the dipole. In the transition region, the hole spacing and hole radius are graded to 0.75 of their nominal values in order to reduce back reflections [51]. More precisely, the hole spacings and hole radii in the transition region are scaled by $[0.95, 0.86, 0.8, 0.75]$ (moving in the $+\hat{x}$ direction) from the values in the waveguide region. (b) Normalized radiated spectra of the dipole into waveguide and non-waveguide radiation channels. (c) Normalized radiated spectra of the dipole into the principal directions of the simulation domain.

where $n_g(\omega)$ is the frequency dependent group index of the waveguide mode, $E(\mathbf{r})$ is the waveguide mode field amplitude, and A is the waveguide mode area defined by

$$A = \frac{1}{a_o} \frac{\int_u d\mathbf{r}\, n^2(\mathbf{r}) |E(\mathbf{r})|^2}{\left(n(\mathbf{r})^2 |E(\mathbf{r})|^2 \right)_{\text{max}}}, \tag{4}$$

where volume u is a unit cell of the waveguide. We have assumed that the dipole and waveguide field at $\mathbf{r}_{\text{NV}}$ are parallel. $|s(\omega)|^2$ is normalized by the "bulk" power spectral density of the NV dipole embedded far below an unpatterned diamond surface. Equation (3) indicates that coupling into a given waveguide mode can be increased by maximizing n_g/A. Photonic crystal waveguides are ideally suited in this regard [55]: they can support modes with sub-wavelength modal area and large n_g.

To gain a quantitative estimate of the NV-waveguide coupling, and to study enhancement or suppression of NV coupling into other radiation modes of the waveguide structure, it is useful to conduct FDTD simulations of the emission spectrum of a broadband dipole source positioned at $\mathbf{r}_{\text{NV}}$. Here we consider a broadband dipole, polarized along $\hat{y}$ and located $z_{\text{NV}} = 11$ nm below the diamond surface and midway between two holes of the photonic crystal waveguide studied

in Sec. 2.1. In order to channel the dipole emission into a forward propagating waveguide mode, the hole spacing of the waveguide structure used here is asymmetric about the dipole position, as shown in Fig. 7(a). For $a_o > a_c$, the valence band edge of this structure is lower on the left side of the dipole than on the right side; the band edge of the left ("mirror") region has a lower frequency than the band edge of the right ("waveguide") region. For efficient collection of NV emission, the structure should be designed such that the majority of the NV phonon sideband emission is lower in frequency than the "waveguide" TE-1 valence band edge, and higher in frequency than the "mirror" TE-1 valence band edge. Note that reflections from the waveguide termination can dramatically alter the coupling between a dipole and the waveguide, as studied in [55]. Here we have chosen a termination designed to suppress these reflections in the simulations. In FDTD simulations of periodic structures supporting propagating modes, PML terminations of the propagating axis can create significant reflections. A waveguide which is invariant along the propagating dimension, such as the termination region of the structure considered here, is better suited for a PML boundary.

Figure 7(b) shows the FDTD calculated spectrum for the system described above. Power spectral density of radiation into the waveguide, and into all other channels (e.g., the substrate) are shown. In the simulations studied here, $a_c = 141$ nm and $a_o = 160$ nm. The hole radius and waveguide cross-section are the same as in Sec. 2.1, and $h = 4a_o$. The spectra are normalized by the spectrum of the identical dipole source when it is positioned at depth z_{NV} below an unpatterned diamond surface. From Fig. 7(b), we see that for frequencies below the valence band edge of the waveguide region ($\omega < \omega_X^{TE-1} \sim 0.25 \times 2\pi/a_o$), the emission into the waveguide exceeds the total "bulk" emission in absence of the waveguide. The radiated waveguide power was calculated by monitoring the power flux through an area overlapping the waveguide cross-section, with dimensions $2w \times 2d$, located near the simulation PML boundary. Note that emission into non-waveguide modes is also enhanced. As shown in Fig. 7(c), radiation into the substrate ($-\hat{z}$ direction) and into the waveguide ($+\hat{x}$ direction) are the dominant radiation channels. Also, note that relatively little power is coupled into the backward propagating waveguide mode ($-\hat{x}$ direction) in the displayed frequency range. For $a_o = 160$ nm, the bandwidth of this efficient waveguide coupling is approximately $637 - 700$ nm, allowing efficient collection of a large portion of the NV$^-$ zero phonon line and phonon sideband emission. This may be particularly useful in room-temperature NV experiments which do not rely upon readout of a sharp optical ZPL, but require efficient collection of sideband emission, for electron spin readout, for example.

2.5. Fabrication considerations

Fabrication of the devices studied in this paper requires three key processing abilities: (i) patterning GaP or another high index film with the design presented above, (ii) attaching high index films to a diamond substrate, and (iii) transferring the thin film pattern into the diamond substrate. Proofs of principle of these individual steps have been demonstrated. Results presented in Refs. [33, 24] show that it is possible to lithographically define and etch sufficiently small holes using current electron beamwriting and plasma etching tools. Large area patterned GaP films were transferred and adhered [56] onto a diamond sample in Ref. [30], as have smaller micron-scale structures [57]. Transferring the pattern into the diamond can be accomplished using oxygen based plasma etching, e.g., in Ref. [54] a highly selective plasma etch was used to extend a SiN pattern into a diamond substrate. The degree to which the precise design studied in Sec. 2.2 can be replicated will affect the maximum achievable Q, and achieving the high aspect ratio diamond sidewalls of the $h = 640$ nm structure may be challenging. Theoretical studies analyzing the importance of the sidewall slope may be necessary in future work. Finally, note that although precise (2 nm) tuning of a_c was considered in Sec. 2.2 in order to maximize Q,

the cavity supports modes with $Q > 5 \times 10^5$ over the range 132 nm $\leq a_c \leq$ 150 nm.

The GaP-based cavity proposed here is designed specifically for coupling to negatively charged NV centers positioned within 50 nm of a diamond surface. It is well established that a dense layer of NV centers close to a diamond surface can be created in high-nitrogen diamond by ion implantation and annealing [58, 59, 60, 54]. Such a dense layer is well-suited for initial testing of the optical characteristics of GaP-based microcavities. However, for the proposed devices to be useful for quantum information applications, single NV centers with good spectral characteristics must be fabricated close to a surface in high-purity diamond. Initial tests suggest that in high-purity diamond, a nearby surface can have a large effect on NV properties [54] that include charge stability and optical linewidth. A thorough study of how to optimize the properties of single NV centers close to a surface will be required for any device based on NV centers coupled to an optical microcavity, including the GaP-based design presented here.

3. Conclusion

In this paper we have analyzed a photonic crystal geometry which supports low-loss, subwavelength nanocavities and waveguides suitable for coupling to diamond NV-centers in single crystal diamond. The structures presented here can be fabricated using existing materials and processing techniques, and promise to allow efficient collection of photons emitted from NV-centers, a crucial requirement for proposed applications [9]. Efficient collection of NV ZPL emission is necessary for single photon and quantum repeater applications of NVs, and efficient collection of NV sidebands is required for high bandwidth readout of the NV electron spin. The photonic crystal nanocavity design presented above supports modes with the necessary Q and V to reach the strong coupling or large Purcell factor regimes with the ZPL of an NV-center. The photonic crystal waveguide analyzed here allows broadband collection of NV emission, and is promising for efficient collection of NV sidebands. In future work, it is expected that integration of multiple cavities, and realization of nanophotonic circuits for quantum information processing using NV-centers, will be possible using the device designs presented here.